Numerical study of the impact of tailored porous media design on syngas production from methane-rich combustion

Yann Roussel*, Pierre-Lou Billerot, Romain Lemaire, Patrice Seers

Department of Mechanical Engineering, École de Technologie Supérieure, 1100 Notre-Dame Street West, Montreal, QC, H3C 1K3, Canada

HIGHLIGHTS

- A 3D pore-resolved CFD model of a diamond lattice-based porous burner is proposed.
- A new tailored graded geometry was tested and compared to isotropic matrices.
- The energy recirculation efficiency was maximized with a higher specific surface.
- The methane-to-syngas conversion ratio was maximized with the graded geometry.
- The graded matrix led to low levels of soot precursors due to a longer oxidation zone.

ARTICLE INFO

ABSTRACT

This numerical study investigates the impact of four proposed porous burner designs, which are based on a diamond lattice structure similar to what could be obtained with additive manufacturing technology, on H_2/CO syngas production. The performances of all the burners were compared, and the results showed that for a given porosity, the recirculation efficiency increased with increasing the pore density. Decreasing the porosity by a factor 2 increased the recirculation efficiency thanks to the presence of higher thermal inertia and local temperature, which allowed to achieve a 53% fuel conversion. Promising results were obtained with the new linearly varying pore diameter matrix, with an observed conversion efficiency of 63% and a reduction in the soot precursor production. This latter behavior itself resulted from an increase in the size of the reaction zone, where elevated temperatures led to high concentrations of H_2 and to the partial oxidation of C_2 species.

Introduction

Syngas is a valuable flammable gas mixture, consisting of hydrogen (H_2) and carbon monoxide (CO), which can be used as a fuel, or as a chemical feedstock (when the H_2/CO ratio is close to unity) in the production of synthetic fuels, alcohols, etc. [1]. Syngas is produced mainly from fossil fuels (oil, gasoline, coal), and to a lesser extent, from biomass [2]. Syngas can notably be produced from the partial oxidation of methane under fuel-rich combustion conditions (CH_4 + ½ O_2 → CO + 2H_2), noting that other routes, such as the dry

---

Please cite this article as: Roussel Y et al., Numerical study of the impact of tailored porous media design on syngas production from methane-rich combustion, International Journal of Hydrogen Energy, https://doi.org/10.1016/j.ijhydene.2022.09.266

methane reforming reaction ($CH_4 + CO_2 \rightarrow 2H_2 + 2CO$) and the water-gas shift reaction ($CO + H_2O \rightarrow CO_2 + H_2$) can play a significant role in the reforming efficiency [3]. In the presence of a catalyst, steam reforming of methane remains the most common way to generate syngas, although it is an endothermic reaction taking place at a relatively high temperature (~1000 K) [4]. In the review by Ref. [2], combustion in porous media (CPM) is identified as a promising approach that does not require a catalyst to produce syngas and H_2. In CPM, the combustion is confined within a highly porous medium (foam, beads, etc.) [5] while some of the heat produced during this process is transferred and conducted through the solid, and preheat the incoming fuel-air mixture by heat convection. This preheat of the fluid also increases the flame temperature. As the present work proposes a numerical study of four porous media used to convert a methane-rich mixture to syngas, a short survey on methane conversion and modeling approaches is presented.

Experiments reported in the literature illustrate the diversity of porous media used to produce syngas. For example, experiments using sponge-type matrices have shown syngas production with H_2/CO ratios between 1.5 and 1.9 with methane-rich mixtures having equivalence ratios (φ) lying between 2.5 and 2.9 [6,7]. Another approach considered stacked pellets or beads to obtain a porous medium. This approach was used by Dai et al. [8] to create a divergent packed burner aimed at decreasing the velocity of the gas for a greater flame stability. From the authors' numerical parametric study, a φ of 2 was shown to offer a higher methane-to-H_2/CO energy conversion efficiency. Fay et al. [9] experimentally compared a packed bed to a reticulated porous ceramic burner and with the latter, observed a significant increase in the methane-to-hydrogen conversion rate. They suggested that this higher conversion rate could be attributable to the higher interstitial velocity and temperature obtained with a reticulated ceramic. Irrespective of the nature of the porous medium used, other experimental studies from the literature have found consistent results, with the methane reforming efficiency maximized at an equivalence ratio close to 2 [10–12].

While different methods can be used to simulate CPM, and to some extent, syngas production, many recent studies have used one of two modeling approaches. The first approach is the volume-averaged method (VAM), which is often used in the literature, based on the survey of [13]. With this technique, the porous burner is defined based on its main characteristics, such as the porosity, but lacks the physical microscale description of the medium. Thus, 1D [14,15], 2D [3,16,17], and more rarely, 3D [18] models are used, and the results do not allow to obtain information such as how the solid and fluid interact at a smaller scale. However, the approach has the advantage of having a low computational cost. The second approach consists of a pore-scale simulation, and involves a more in-depth modeling of the physical structure and of its interaction with the fluid in combination with reduced or detailed kinetics. With pore-scale simulations, 2D [19] and 3D [20–23] techniques are used. With regard to the 2D simulations, Shi et al. [19] modeled a two-layer burner consisting of 2.5 mm and 7.5 mm beads in the upstream and downstream sections, respectively, and considered the effect of adding CO_2 to a rich methane-air mixture. They observed a decrease in H_2

production and an increase in CO production as CO_2 was added to a rich methane-air mixture. With the 3D model approach, either a single column [20,23] or an entire burner [21,22] can be modeled. In both cases, the approach has the advantage of capturing small-scale phenomena such as spatial velocity fluctuations, a task that is not possible with the volume-averaged method. For example, Yakolev and Zambalov [21] modeled a 3D random packed spheres burner with a rich methane-air mixture having a φ of 2.5. Observations at the pore scale revealed large spatial variations of the temperature and velocity fields due to the inhomogeneity of the matrix. Moreover, they analyzed the fluid-solid interactions leading to unsteadiness of the front flame at the pore level.

While the porous burner is made of foam or pellets/beads in the above literature survey, new designs are proposed such as a porous radiant burner where the combustion takes place within a volume confined by a porous structure having a high pore density (porosity close to 65% and 30-70 pores per inch (PPI)) [24–26]. This approach, named internal combustion regime (ICR), is said to offer radiant efficiency greater than 50% without mixture preheat [24]. Other recent approaches based on the idea of using tailored porous structures has recently emerged as a potential application to CPM [27,28]. One example of a tailored design is the biomimetic inspired leaf-type hierarchical porous medium studied by [4] for solar driven methane reforming. By optimizing the solar porous reactor with respect to temperature distribution, such a leaf-inspired structure resulted in a 7% improvement of methane conversion to syngas [29]. The idea of designing structured media with a controlled morphology is driven by the possibility of making them using advanced manufacturing techniques such as additive 3D printing technology [30]. Such an approach has been used by Samoilenko et al. [27] who designed and printed porous media based on a diamond lattice matrix. Their experiments showed the advantage of using diamond lattice structures as compared to foam as the former offer better resistance to deformation and thermal shock. In the present study, investigations are pursued with the objective of evaluating the influence of the porosity and pore diameter of a diamond lattice medium when used to produce syngas from a methane-rich mixture. The effect of porosity is addressed by comparing two media having the same pore diameter but very different porosity (86% vs. 44%) while the impact of pore diameter is tackled by comparing two media having a constant porosity but with pore diameter of 1.8 and 3.1 mm. Moreover, a new design is proposed using a linearly varying pore diameter which is compared to isotropic matrices having a constant porosity and pore density. The comparison is based on the heat recirculation efficiency and the methane to syngas (H_2/CO) conversion efficiency while the production of C_2 soot precursors is also assessed. These parameters are used to illustrate the advantage of the proposed new design.

Methodology

Geometry and computational domain

In this work, different geometries of porous burners are studied following the work of Samoilenko et al. [27], in a bid to

obtain a regular porous medium based on a diamond lattice matrix. As the objective is to quantify the burner operation, four different designs are compared. In order to facilitate comparisons with a foam burner, diamond lattice structures having equivalent porosity and permeability to a 10 and a 30 pores per inch (PPI) foams (porosity of 82% and 86%, respectively) are studied and are identified as cases A and B, respectively. Their main properties are shown in Table 1. The impact of the pore diameter, at a quite constant porosity, is achieved by comparing case A to case B, while the effect of the porosity is numerically studied by comparing case B to case C. Finally, case D shows an example of the advantage offered by printing technology by presenting a medium with varying pore diameter from the inlet to the outlet of the burner.

Although the shape of the lattice is maintained, the geometric parameters of the matrix, such as the strut thickness and the cell size, are changed from one case to another. Their values are given in Table 1, while a single lattice is presented in Fig. 1 illustrating the difference between a cell (a sphere encased within a diamond lattice) and a pore (a disk encased within a hexagon made from the struts of a diamond lattice). In the modeling effort presented herein, a single column taken at the center of a would-be 5 cm high burner is used. Fig. 2 shows a single unit of the lattice structure (left) and the resulting CFD model (right).

Numerical setup

The numerical model is similar to the one implemented in the work of Billerot et al. [20]. It uses a two-energy equation model, one for the gas and one for the solid, as the two phases are in non-thermal equilibrium. Heat transfer is carried out by convection between the fluid phase and the solid matrix. The porous medium is assumed to be homogeneous and inert while the solid has the thermo-physical properties of silicon infiltrated silicon carbide (SiSiC) adopted from [20]. The properties are assumed constant and thus independent from the solid temperature due to a lack of data or correlations.

The proposed CFD model considers the fluid flow as being laminar while behaving as an ideal gas. The reactive gas mixture is perfectly premixed at the inlet and the thermophysical properties of the gas depend on the temperature and species concentration as defined in the GRI-Mech 1.2 [31], which is the reaction mechanism used herein. Additionally, the Dufour and Soret effect are neglected.

Based on the above assumptions, the set of differential equations governing the physics is presented, and Eq. (1) first describes the mass conservation:
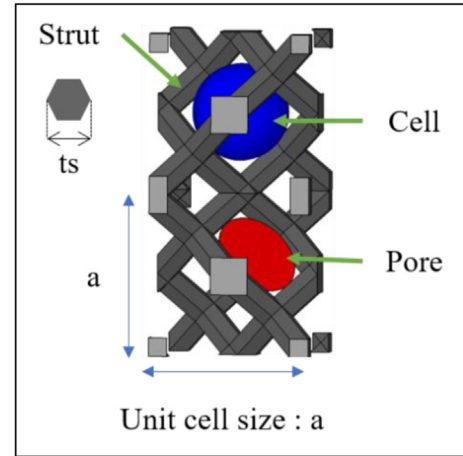

Fig. 1 — Geometric parameters.

$$\frac{\partial}{\partial t}\left(\rho_f\right) + \nabla \cdot \left(\rho_f \overrightarrow{u}\right) = 0 \tag{1}$$

where $\overrightarrow{u}$ is the velocity vector and ρ_f is the gas density. For a multi-component mixture, ρ_f is computed with the ideal gas law (Eq. (2)):

$$\rho_f = \frac{P}{RT} \frac{1}{\sum_{k=1}^{n} \frac{Y_k}{W_k}} \tag{2}$$

where P is the static pressure, T_f the fluid temperature and R is the universal ideal gas constant. For each species, k, Y_k and W_k represent the mass fraction and molecular mass, respectively. The momentum equation presented by Eq. (3) can be written:

$$\rho_f\left(\frac{\partial \overrightarrow{u}}{\partial t} + \overrightarrow{u} \cdot \nabla \overrightarrow{u}\right) = \nabla P + \nabla \cdot \left(\overline{\overline{\tau}}\right) \tag{3}$$

in which $\overline{\overline{\tau}}$ is the viscous stress tensor. The conservation of energy in the fluid is represented by Eq. (4):

$$\frac{\partial}{\partial t}\left(\rho_f C_{p_f} T_f\right) + \nabla \cdot \left(\rho_f C_{p_f} T_f v\right) = -h_{conv}(T_f - T_s) - \nabla \cdot \left(k_f \nabla T_f\right) - Q_{ch} \tag{4}$$

where Q_{ch} is the rate of heat release from the chemical reactions defined as $Q_{ch} = \sum_{k}(\dot{\omega}_k h_k W_k)$. As for $\dot{\omega}_k$, it stands for the rate of production/consumption of the kth species, while h_k and W_k are its molar enthalpy and molecular weight, respectively. The gas-specific heat, C_{p_f}, has been calculated using the mass-weighted mixture method, while the thermal

Table 1 — Description of the geometric characteristics of the matrices and inlet conditions.

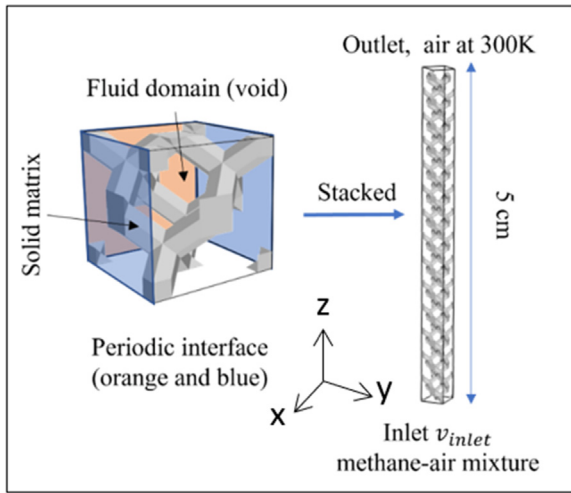| Case	Pore density (PPI)	Porosity (%)	Strut thick. (mm)	Pore dia. (mm)	Cell dia. (mm)	Surf/Vol. (m^{-1})	Eq. ratio (−)	Inlet vel. (cm/s)
A	8.2	82	0.95	3.1	4.5	508	1.5 and 2	17
B	14.1	86	0.69	1.8	2.6	865	2	28
C	13.4	44	2.2	1.9	2.7	726	2	14
Lower porosity								
D	13.4—6.9	86	0.69—0.88	1.9—3.7	2.6—4.2	793	2	15
Variable pore dia.								

Fig. 2 – **Description of the geometry and boundary conditions. Left: CAD model of a unit cell; Right: CAD model of the column for CFD calculations.**

conductivity follows the Mathur-Saxena averaging method based on the mole fractions of the different species [32]. Then, the energy conservation in the fluid is expressed as per Eq. (5):

$$\frac{\partial}{\partial t}[\rho_s C_s T_s] = \nabla \cdot [k_s \nabla T_s] + h_{conv}(T_f - T_s) - \nabla \cdot \overrightarrow{q}_{rad} \tag{5}$$

where C_s, T_s, k_s, and ρ_s represent the heat capacity, the temperature, the conductivity, and the density of the solid phase, respectively. Both energy equations (Eqs. (4) and (5)) are coupled by the heat convection coefficient, h_{conv}, modeled with a conjugate heat transfer boundary condition at the fluid-solid interface.

In the fluid energy equation (Eq. (4)), gas radiation has not been considered following [20], while the solid matrix is regarded as a gray and homogeneous medium that can absorb, emit or scatter radiation. The radiative heat flux $\nabla \cdot \overrightarrow{q}_{rad}$ appearing in Eq. (5) is calculated with Eq. (6):

$$\nabla \cdot \overrightarrow{q}_{rad} = \int\limits_{0}^{+\infty} \alpha_\lambda \left[4\pi I_{b_\lambda} - \int I_\lambda(\Omega) d\Omega \right] d\lambda \tag{6}$$

where α_λ is the absorption coefficient at the wavelength λ, and I_{b_λ} is the spectral intensity of a black body evaluated using the Plank's law. The transport of the radiant intensity for a specific wavelength is governed by the radiative transfer equation (RTE) defined in Eq. (7):

$$\frac{dI_\lambda}{ds} = \alpha_\lambda I_{b_\lambda} - (\alpha_\lambda + \delta_\lambda) I_\lambda + \frac{\delta_\lambda}{4\pi} \int\limits_{4\pi} I_\lambda(\Omega) d\Omega \tag{7}$$

where δ_λ is the scattering coefficient. The matrix acts as a homogeneous gray medium and α_λ likewise δ_λ are considered as independent of the wavelength. One can add that this equation was solved using the discrete ordinate method.

Lastly, an equation for the species conservation is used (Eq. (8)):

$$\frac{\partial}{\partial t}[\rho_f Y_k] + \nabla \cdot [\rho_f Y_k \overrightarrow{u}] = \nabla \cdot [\rho_f D_{k,m} \nabla Y_k] + \dot{\omega}_k W_k \tag{8}$$

where $D_{k,m}$ is the diffusion coefficient between species. The diffusive flux was evaluated based on the Fick's law using the kinetic theory for the calculation of the molecular diffusivity of the species k in the mixture.

Boundary conditions

For the single column burner illustrated in Fig. 2, the following boundary conditions are imposed on the fluid phase: at the inlet, a perfectly premixed methane-air gas mixture is injected at a constant velocity to ensure a stable flame within the burner; thus, $u_x = u_y = 0$; $u_z = u_{inlet}$; $Y_i = Y_{i,\varphi,0}$; $T_f = T_0 = 300\,K$. At the outlet, a zero normal gradient is imposed on the specie mass fractions and temperature while the pressure is set to one atmosphere. In the solid, radiation with the environment at 300 K is applied at the inlet and outlet faces and is expressed as $q_{rad,out} = -\varepsilon\sigma(T_s^4 - T_0^4)$, where σ is the Stefan-Boltzmann constant. At the fluid-solid interface, a no-slip condition is applied. Finally, on the four lateral sides of the computational domain, a periodic boundary condition is used to ensure solution continuity of the solid and fluid phases, so that only a single column of the burner is modeled, as illustrated in Fig. 2.

Solution method

The calculations are conducted with the commercial CFD software STAR-CCM+. The SIMPLE (Semi-Implicit Method for Pressure-Linked Equation) algorithm is employed to solve the coupling between the pressure and the velocity in the momentum equation. A second-order implicit formulation is used for the temporal discretization with a time step of 10^{-5} s. A second-order upwind scheme is used for the spatial discretization. The equations are solved and a convergence criterion of 10^{-5} is required especially for the energy residual [20]. Computations were carried out on the Graham supercomputer managed by Compute Canada.

Grid Independence and Numerical Model Validation

A mesh independence study was first conducted to determine the impact of the mesh refinement on the solution. The study consisted in modeling an isothermal airflow at 300 K in order to validate the pressure drop along the porous matrix. Thus, different mesh densities were tested using the geometry of the reference case A. The mesh study was conducted in two steps. The first consisted in evaluating the influence of the mesh size without using prismatic layers, with a polyhedral mesh size that is gradually increased from about 500,000 to 7.6 million. As can be seen in Fig. 3, the relative error decreases toward a minimum as the number of cells increases.

In order to reduce the relative error on the pressure loss, the second step looked at the impact of adding prismatic layers to the mesh. The thickness of the prismatic layers was set to 5% of the strut diameter, and the number of layers was varied from 1
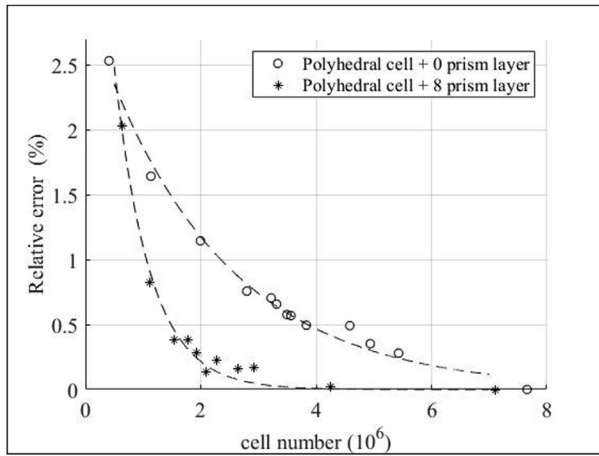
Fig. 3 — Mesh convergence study.

to 10. This prismatic layer sensitivity study was conducted on 3 different meshes: coarse (~1 million cells), medium (~2 million cells) and fine (~3 million cells). The results showed that 8 prismatic layers resulted in a good convergence of the numerical results and thus more mesh sizes were studied. Fig. 3 presents the impact of the number of cells for a constant 8 prismatic layer. When considering the computation time and the relative error on the pressure drop, a mesh with 2.8 million cells, including 8 prismatic layers, was chosen as a good compromise with a 0.2% relative error.

Based on this choice, the mesh configuration was applied to cases A and B, and a validation was conducted with a non-reacting flow through the porous medium, with inlet velocities ranging from 1 to 40 cm/s. The results were compared to the Darcy-Forchheimer pressure drop law using the correlations proposed by Ergun [33], Fand [34] and Du Plessis [35] based on the porosity (ϕ), pore diameter and tortuosity, as shown in Fig. 4. The Darcy velocity u_D, also called the superficial velocity, can be defined as $u_D = \phi u_z$, with u_z being the average pore flow velocity.

As illustrated in Fig. 4, the results, having a quadratic form in both cases, are close to the literature correlations. The results in case A are in very good agreement with the correlations

proposed for different types of porous media (foam or beads) and different porosities (maximum relative error of ~3.7% with respect to [33]). Although a more significant deviation with the correlation's predictions is observed for case B (relative error of ~13% with [33]), the results from the proposed model lie somewhere in-between the correlations of [33] and [35]. It is eventually observed that the pressure drop is higher for matrix B because of its higher pore density as compared to matrix A.

From convergence and isothermal flow study results, it can be stated that the proposed mesh is suitable for predicting the flow characteristics. The characteristic average mesh sizes in the fluid phase for cases A and B are 80 μm and 65 μm, respectively. Details of the mesh for the different geometries tested in this study are presented in Table 2. Since the geometries of cases C and D are based on cases A and B, respectively, the same meshing approach is used in all cases. In addition to the fluid domain, the solid domain must be meshed, and is constrained by the choice of the fluid region mesh. Due to the refinement of the cells at the interface, the solid cells have an average size of 81 and 68 μm for cases A and B, respectively.

To complete the model validation, the influence of the equivalence ratio was studied to see the response of the model using φ values of 1.5 and 2 with the geometry of case A. To this end, the scalar fields of CO and H_2 mole fractions plotted on a median plane from 1.5 cm to 5 cm are presented in Fig. 5 for both conditions.

In first observing the formation of CO (column on the right) at an equivalence ratio of 1.5, a high CO concentration spot is located in the reaction zone, and is then partially oxidized by residual oxygen to form CO_2. This CO concentration peak is not visible at an equivalence ratio of 2 (case A), where CO is formed more gradually. Eventually, the mole fraction of CO produced is, as expected, higher at an equivalence ratio of 2. Furthermore, when comparing the concentrations of CO and H_2 at the burner outlet for an equivalence ratio of 1.5 to the experimental results of Zeng et al. [3] obtained with beads, a good concordance is noted. Indeed, the model predicts CO and H_2 concentrations and a maximum gas temperature of 8.3%, 8.5%, and 1813 K, respectively, while experimental values of 7.8% for both species and a gas temperature of 1880 K are reported in [3]. Similarly, the values of CO, H_2 and the maximum gas
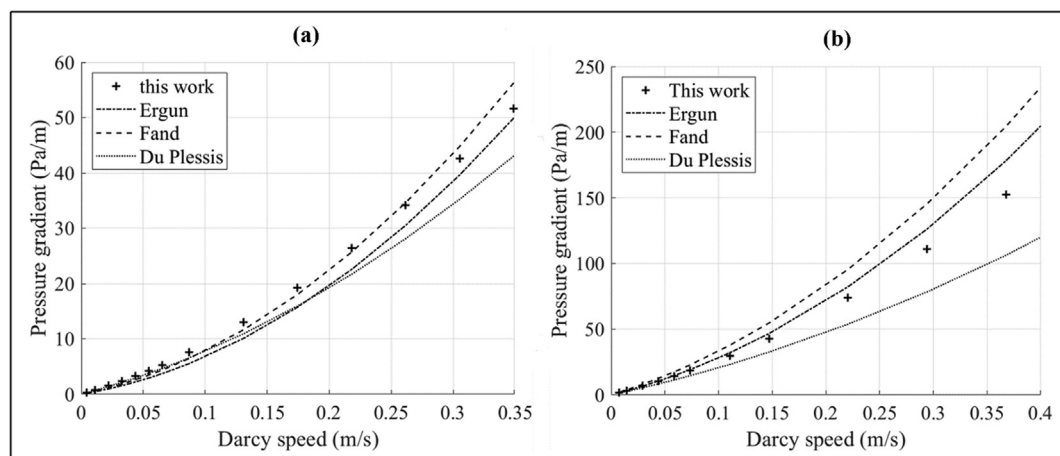

Fig. 4 — Validation of the macroscopic pressure gradient with pressure drop law correlations: (a) Case A; (b) Case B.

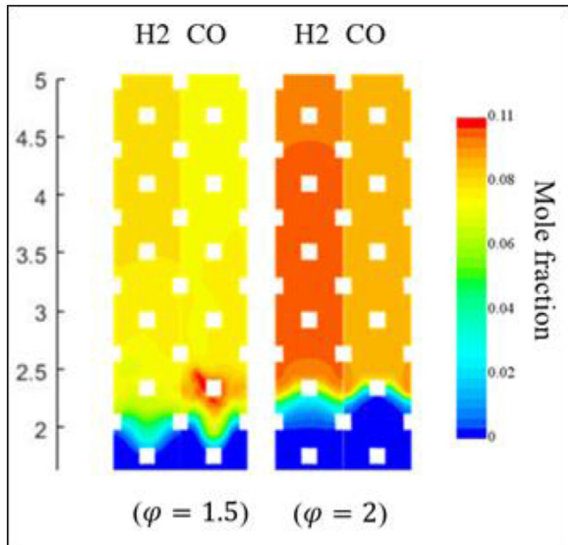| Table 2 – Mesh characteristics.						
Case	Fluid cells (10^6)	Solid cells (10^5)	$\overline{d}_{fluid}$ (µm)	$\overline{d}_{solid}$ (µm)	$d_{min,fluid}$ (µm)	$d_{max,fluid}$ (µm)
A	2.8	4.2	80	81	5	372
B	1.9	3.7	65	68	5	336
C	1.9	6.7	73	112	7	324
D	1.9	3.5	66	72	7	388

Fig. 5 – Influence of the equivalent ratio on CO and H_2 scalar fields for geometry A at an equivalence ratio of 1.5 (left) and 2 (right).

temperature obtained by the model at an equivalence ratio of 2 (9.4%, 11%, and 1804 K, respectively) are in concordance with the 2D numerical results (VAM and skeletal kinetic mechanism) of Dai et al. [8], who obtained 10%, 12%, and 1641 K respectively, using a cylindrical pellets bed.

From the above results, the model shows a very good agreement with the pressure loss correlation of [33] as well as with experimental specie concentrations (maximum relative error of 9%) and maximum gas temperature (relative error of 3.6%) of [3]. Thus, the model is used as is thereafter.

Results

In the following sections, four designs exhibiting varied pore diameter and porosity are compared, while a burner with varying pore diameter is also studied. The equivalence ratio is kept constant and equal to 2, but the inlet mass flow rate is adjusted similarly to Bubnovich et al. [36] for each case in order to provide a stable flame or quasi-steady state with respect to the species, heat release rate and temperature profiles at the macroscopic scale. It could be said that the inlet velocity presented in Table 1 is close to the lowest value ensuring a stable burner operation. Indeed, the macroscopic thermal wave can propagate within the matrix on a time scale of 10^1–10^2 s although the phenomena at the pore scale are unsteady and local fluctuations are observed [21]. The analysis first emphasizes phenomena at the macroscale such as the flame structure, heat recirculation and flow in the burner. Then, the paper highlights the influence of the matrix design parameter on syngas production and pollutant formation.

Flame structure

As the flame stabilizes in the burner around a quasi-steady position, three zones can be identified when looking at the fluid and solid temperature profiles and the heat release rate (HRR) curve as shown in Fig. 6 for case A. The results are mass flow-averaged at every 0.5 mm using 100 planes over the height of the column. The first region corresponds to the preheat zone, where the matrix temperature is higher than that of the unburned gas mixture. In this region, heat is transferred from the solid to the gas by convective heat transfer. At a height of 2.19 mm, the reaction zone begins. This position matches the location where 1% of the peak of HRR is released. Within the reaction zone, the gas temperature is higher than that of the solid due to exothermic reactions.
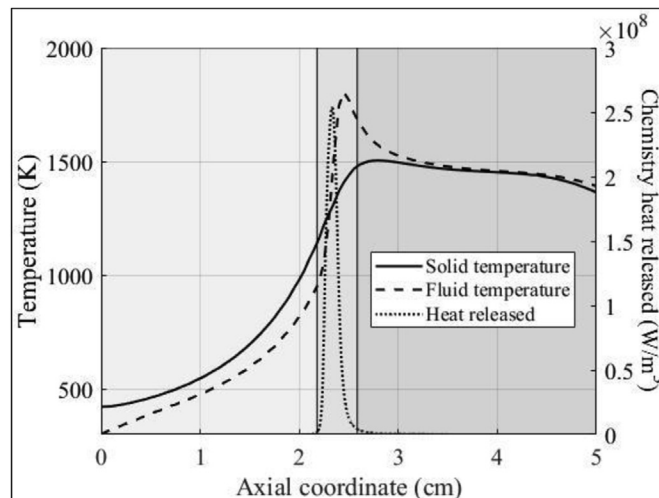

Fig. 6 – Temperature and HRR profiles related to case A.

Consequently, heat is transferred from the gas to the matrix by convective heat transfer. The third region corresponds to the post-flame zone, where both phases reach a thermal equilibrium. This region extends from the end of the reaction zone to the burner exit plane. In the vicinity of the burner outlet, an inflection of the temperature is visible because of the heat losses by radiation with the environment at 300 K.

Heat transfer and energy recirculation

The above description is linked to the heat recirculation phenomenon commonly observed in CPM [37]. Fig. 7 presents the non-dimensional volumetric convective heat transfer, defined with respect to the highest value of case B, from the gas to the matrix for cases A, B and C.

The three zones described in section Flame structure can also be identified in Fig. 7 since the preheat zone is dominated by the heat transfer by convection from the solid to the gas. The heat transfer is negative according to the sign convention adopted herein. Following this energy transfer to the gas, a positive heat transfer (thus, gas to solid) is observed and results from the higher gas temperature due to combustion in the reaction zone. Then, the heat transfer in the post-flame zone is almost zero because a thermal equilibrium between the solid and the gas is reached. The heat recirculation is induced by radiative and conductive heat transfers within the solid phase. The energy gained by the solid from the gas in the reaction zone is then partly transferred upstream in the preheat zone by both mechanisms and increases the solid temperature. Simultaneously, heat transfer by convection in the upstream region increases the entrant gas temperature. The fraction of heat recirculating in the burner can be quantified by calculating the preheat efficiency defined as the ratio between the heat transfer from the solid to the fluid in the preheat zone and the total amount of heat release. From this definition, efficiency of 43%, 53% and 63% is obtained for cases A, B and C, respectively, illustrating the impact of the pore density (case A vs. case B) and porosity (case B vs. case C) on the preheating process. This enhancement of the preheat

efficiency with a higher pore density is mainly due to the high surface-to-volume ratio of the B medium (see Table 1) as the porosity of matrices A and B is similar. The net consequence of a higher pore density is a higher amount of energy transferred from the reaction zone to the preheat zone. The width of the preheat zone in case B is also larger, as shown in Fig. 8 that presents the temperature profiles, which promotes heat transfer to the fluid. For case C, the mass of the burner being higher due to the low porosity, more energy is consequently stored and transferred to the preheat zone. Eventually, the front flame stabilizes close to the outlet (see location of positive heat transfer in Fig. 7), resulting in a larger preheat zone, which contributes to improving the heat recirculation.

Influence of the matrix geometry at the macroscale

Fig. 8 depicts the solid and temperature profiles for three porous geometries tested herein. The maximum flame temperatures were compared in order to look at the impact of the pore diameter at a constant porosity (case A vs. case B) and by comparing the porosity at a constant pore diameter (case B vs. case C). Peak temperatures of 1800 K and 1830 K are obtained for case A and case B, respectively, confirming the presence of a superadiabatic combustion as the adiabatic flame temperature of a methane-air mixture at a φ of 2 is 1630 K. Moreover, the results show that halving the porosity by nearly 2, such as in case C, resulted in a higher peak temperature of 1873 K.

To help explain the differences in maximum temperatures observed, the analysis now looks at the effect of the medium geometry on the reaction zone thickness based on the HRR profile. From the results presented in Table 3, it can be observed that the width of the reaction zone differs with the pore density and medium porosity. As the pore diameter decreases by increasing the number of pores per inch, as in case B, or by reducing the porosity, as in case C, the flame thickness is reduced and a strong relationship between the cell size and the flame thickness is obtained. Indeed, the results suggest that chemical reactions are taking place mainly within a single cell for every porous medium tested herein. Matrices with a
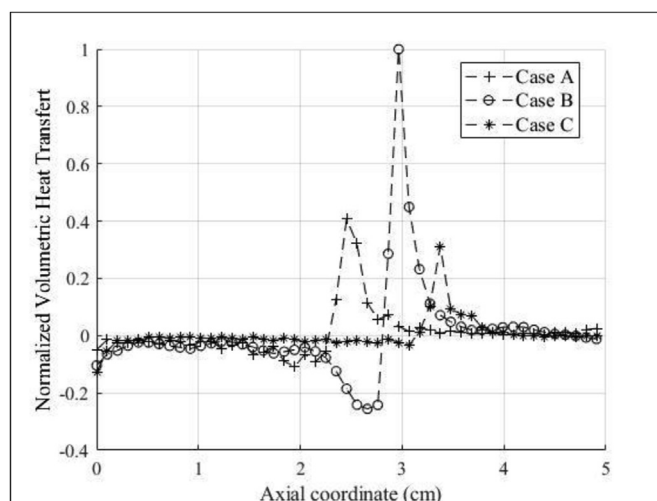

Fig. 7 – Influence of pore diameter (case A vs. case B) and porosity (cases A and B vs. case C) on the gas-to-solid convective heat transfer.
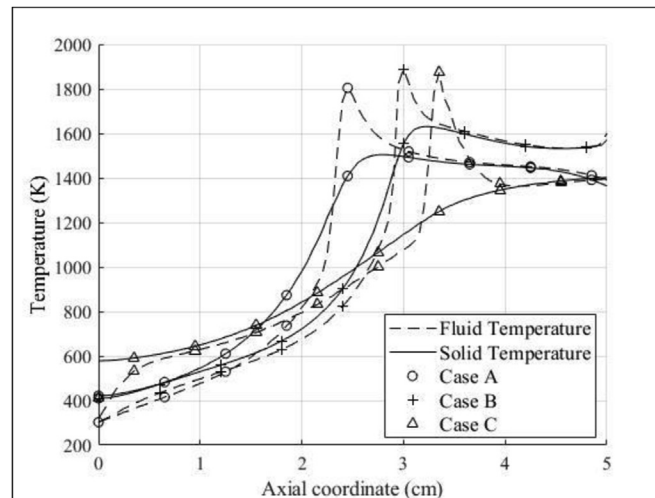
Fig. 8 – Influence of pore diameter (case A vs. case B) and porosity (cases A, B vs. case C) on the temperature profiles.

Table 3 – Influence of the matrix design on the peak temperature, flame thickness and heat recirculation efficiency.

Case	A	B	C
Diamond lattice cell dia. (mm)	4.5	2.6	2.3
Flame thickness based on HRR (mm)	4.5	3.0	2.3
Peak flame temperature (K)	1800	1830	1873
Heat recirculation efficiency (%)	43	53	63

small cell size thus concentrate the heat release in a smaller volume. For example, the maximum heat release per unit volume is about 2.5 times higher with case B due to a smaller cell volume of that medium as compared to case A, although the entering mass flow rate is 1.6 times less. As a consequence, the local flame temperature and temperature gradient are slightly higher for case B as this geometry offers a greater surface area per volume for heat exchange by convection between the solid and the gas (see Table 1, Surf/volume ratio), thus also favoring a higher equilibrium temperature at the outlet (Fig. 8).

Furthermore it is observed, in Fig. 8, that case C has the highest solid and gas temperature in the preheat zone. The low porosity matrix, due to its larger mass, recirculates more energy to the fluid when compared to the other media as was shown in Table 3. Finally, the temperature profiles in Fig. 8 also show that the flame in case C, stabilizes farther downstream, although the gas inlet velocity is the lowest (17 cm/s in case A and 28 cm/s in case B vs. 14 cm/s in case C). This is because the pore and cell sizes are smaller in case C (see Table 1), leading the flow and the front flame to reach a higher velocity at the pore scale, as will be shown in section Flow analysis.

Flow analysis

The preheating of the incoming gas mixture highlighted above increases the unburned mixture velocity due to gas expansion. This ensures flame stabilization within the burner whereas the inlet velocity in case A is equal to 17 cm/s, while it is 28 cm/s in case B and 14 cm/s in case C. These values should be put into perspective considering that a laminar flame speed of 3.9 cm/s is obtained for a freely propagating flame at an equivalence ratio of 2. From this observation, the presence of the porous medium allows attaining maximum burned gas velocities of 1.8 m/s, 3.16 m/s and 2.17 m/s in cases A, B, and C, respectively. This can be observed for cases A and C in Fig. 9 that presents four streamlines of the fluid within the porous
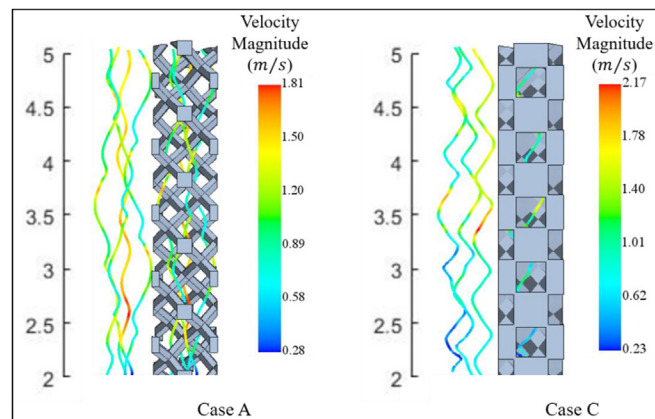

Fig. 9 – Influence of porosity on streamlines: high porosity (case A, left) vs. low porosity (case C, right).

Table 4 — Characteristics of each layer of the variable pore density matrix.			
Layer	Stretching factor	Average Porosity (%)	Equivalent cell dia. (mm)
1	1	86	2,6
2	1.42		2,9
3	1.96		3,2
4	2.62		3,6
5	3.41		3,9
6	4.34		4,2

medium. Although the inlet velocity is lower in case C than in case A, the peak velocity is higher by a factor 1.2 because of the low porosity of the matrix, which results in narrow openings responsible for accelerating the flow. A similar observation can be made by comparing case A to case B (results not shown for brevity), where the higher pore density reduces the cell size.

Nonetheless, a similarity in the flow pattern is observed in all configurations, which is due to a maximum pore Reynolds number ($Re_{p,max}$) of 23–24 for cases A and B, while it has a value of 15 for case C. These values are associated with the laminar Forchheimer regime, which is characterized as lying between a flow dominated by the viscous forces (Darcy regime with $Re_{p,max} < 6$) and a flow where the inertial forces are dominant (nonlinear regime with $Re_{p,max} > 60 - 65$) [34]. The structured nature of the matrix and the laminar regime of the flow translate into a channeling flow, with a limited interaction between the helicoidal-shaped streamlines, as was already observed by Ref. [20].

Variable pore density

To enhance the stabilization range and the heat recirculation efficiency, it has been suggested that a graded matrix geometry can be used [23,28]. Thus, in this section, the effect of linearly varying the pore density along the burner while keeping the porosity equal to 86% (case D) is explored. The

bottom layer has the properties of case B and the 5 upper layers are obtained by stretching the lattice in the z-direction in order to get a top layer having the properties of case A. Thus, the pore density decreases from the inlet to the outlet. In order to keep a 5 cm column with the same mesh base size as in the first layer, the first layer mesh is deformed into a rectangular cuboid having the same cell volume as in case B. The deformation factor of the intermediate stages is obtained by linear interpolation between the two extremities. The characteristics of each section are presented in Table 4. Because of stretching, the cells of the matrix have an ellipsoidal shape. The equivalent cell size shown in Table 4 is calculated from the diameter of a sphere having the same volume.

Temperature profiles

A simulation was conducted at an equivalence ratio of 2 and the results are compared with cases A and B. Fig. 10 presents the solid and fluid temperature profiles for the three cases. Because the new burner has a variable pore diameter geometry, the front flame stabilizes farther downstream. As a consequence, the preheat zone is larger in comparison with cases A and B, resulting in a highly efficient heat recirculation within the matrix. Indeed, the preheat efficiency is 43% and 53% in cases A and B, respectively, while it rises to 59% in case D. Nevertheless, the performances of the low porosity matrix (case C) are better in terms of heat recirculation (63%) because of its higher thermal inertia although the thermal load applied at the burner inlet is roughly 2 times smaller than in case D.

Syngas production

In this section, the main species of syngas production are analyzed using Fig. 11, which presents the scalar field of CO (Fig. 11-left) and H_2 (Fig. 11-middle) mole fractions as well as the fluid temperature (Fig. 11-right). As a first observation, it can be stated that cases A and B (same pore density) do not differ significantly from each other with respect to molar concentrations but differ in flame location. Indeed, the mole fractions of CO and H_2 produced are quite similar although, a modest increase by 5.5% and 2%, respectively, is noted for case
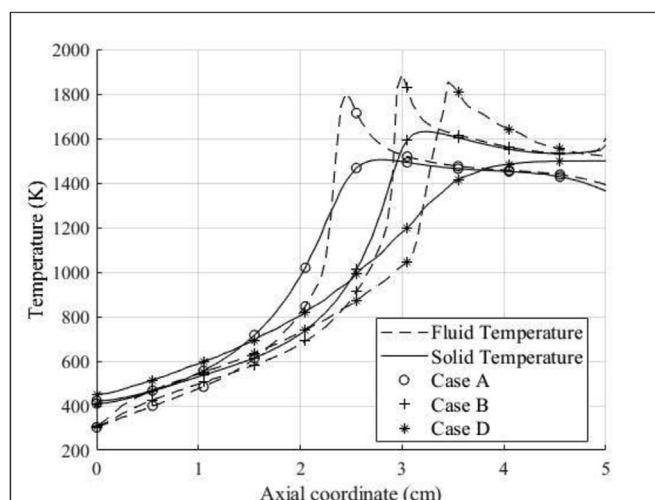

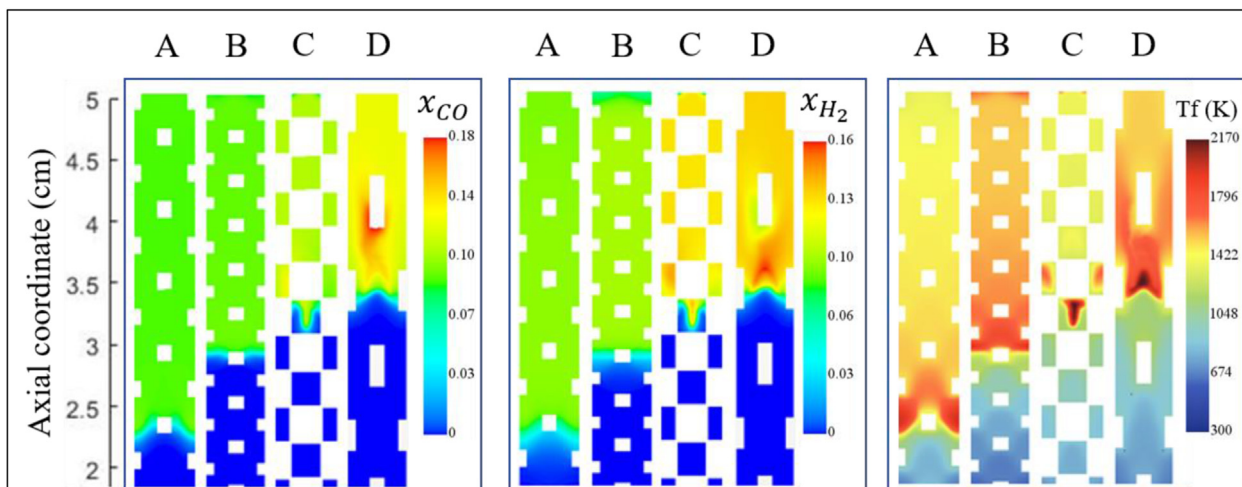**Fig. 10 — Influence of variable pore diameter on temperature profiles.**

Fig. 11 − Scalar fields of CO and H_2 mole fractions together with fluid temperatures for cases A to D.

B. This slightly improves the H_2/CO ratio and the conversion efficiency calculated in Table 5, likely as a result of the higher temperature met in the reaction zone with burner B.

Lowering the matrix porosity has a positive effect on the production of syngas as the conversion efficiency reported in Table 5 for case C (porosity of 44%) is 53%. This thus represents a gain of 10% as compared to case B, which has a similar pore density. This higher conversion efficiency is similar to the experimental results of [11], who observed an efficiency of 50% at an equivalence ratio of 1.7 using a porous burner made up of

pellets with a porosity of 46%. This significant improvement of the conversion efficiency can be attributed to the high local temperature, which reaches 2170 K within a cell of the burner, contributing to producing H_2 and CO at higher levels than in cases A and B. With the pores being small in burner C, no subsequent reactions involving H_2 and CO occur downstream of the main reaction zone.

Stretching the matrix in order to obtain a burner with a graded geometry is even more beneficial for the methane-to-syngas conversion efficiency. Indeed, a high temperature spot is visible in the main reaction zone in burner D, where H_2 and CO are produced. Then, it can be noticed that H_2 is partially oxidized close to a strut of the solid matrix. Meanwhile, at this particular location, CO is formed and reaches a local high concentration. Just ahead of the obstacle, the reverse water gas shift reaction (RWGS: $H_2 + CO_2 \rightarrow CO + H_2O$) is likely dominant since it was also verified that CO_2 is consumed and H_2O is produced. This concept is also supported by the fact that the local temperature drops and the

Table 5 − Influence of the geometry on burner efficiency.

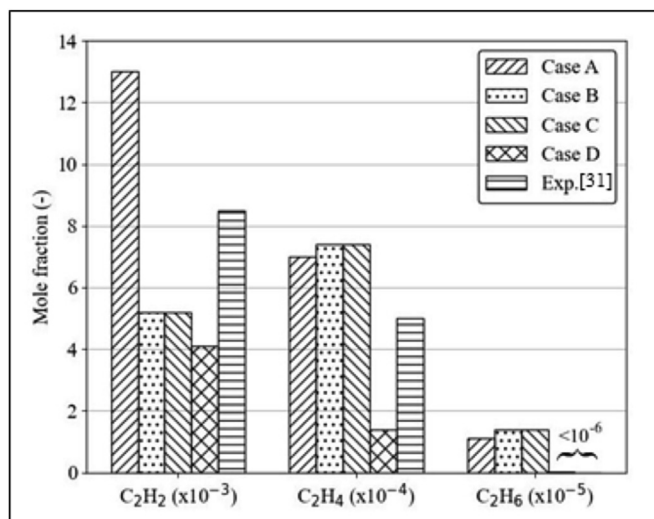| Case	H_2/CO (−)	$\eta_{CH4-syngas}$ (%)	Thermal load (kW/m^2)
A	1.06	41	1361
B	1.13	43	2236
C	1.15	53	563
D	1.06	63	1200

Fig. 12 − Influence of burner geometry on soot precursors at burner outlet.

rate of heat release becomes negative. This was expected since the RWGS reaction is moderately endothermic [19]. However, the H_2 and CO concentrations remain higher than in cases A, B and C, but in the same proportion to case A. Eventually, the conversion efficiency jumps to 63% in case D.

Soot precursor emissions

Burning rich methane-air mixture for syngas production is also accompanied with the production of particulate matter, as observed by Toledo [38]. Thus, our investigation proceeds by looking at the concentration of three soot precursors (acetylene C_2H_2, ethylene C_2H_4 and ethane C_2H_6), for which a comparison is possible with experimental data. The bar chart presented in Fig. 12 shows the mole fractions of these species produced at the burner outlet on a wet basis for cases A to D. A comparison with the experimental results of [38] is performed. The authors in Ref. [38] tested a methane-air mixture at an equivalent ratio of 2 in a porous medium consisting of pellets having a porosity of ~40%.

Overall, in terms of order of magnitude, the species production is consistent with the experimental results of [38]. Nonetheless, a discrepancy of two orders of magnitude is noted for C_2H_6, except for case D, where a negligible amount of ethane is produced, as observed experimentally in Ref. [38].

As a first observation, it would seem that the porosity does not impact the production of soot precursors since their molar fractions are almost equal in cases B and C, at the same pore density but different porosity. Conversely, varying the pore density while keeping the porosity constant leads to significant variations in C_2 production. For example, the production of acetylene in case A is more than twice the value obtained with case B. The model with the new graded geometry tested herein (case D) exhibits a significant decrease in all soot precursors. Even though the level of acetylene is comparable to cases B and C, ethylene production is divided by 5, and at the same time, ethane is cut by 2 orders of magnitude in comparison with cases A, B and C. A possible explanation for this behavior could be the elongated ellipsoidal shape of the matrix cell obtained by stretching the geometry. As a consequence, a long post-oxidation region is formed downstream of the main reaction zone, where the soot precursors can be oxidized [39]. In fact, it was verified in case D that the soot precursors produced in the main reaction zone are then partially consumed with residual oxygen, supporting this idea. In comparison, the oxidation of the C_2 species was not observed in the other cases.

Conclusion

In this study, a 3D CFD model of a novel porous burner based on a tailored porous geometry was presented. The model allowed to study the impact of the matrix characteristics on the production of syngas and soot precursors from a methane-rich flame having an equivalence ratio of 2. The following results were obtained from simulations:

- The flame settled in one open cell of the matrix, resulting in a thinner flame and reaction zone when the pore density

was increased (case B) or the porosity was lowered (case C). A high pore density matrix is characterized by a larger surface-to-volume ratio, which enhances the heat transfer from the solid to the gas, and thus increases the recirculation efficiency from 43 to 53%, as was found in cases A and B, respectively.

- As the porosity is decreased by a factor 2 (case C), the mass of the solid matrix is likewise increased, and so does its thermal inertia. As a consequence, the matrix temperature at the inlet is higher due to less cooling, and the temperature difference between the incoming gases and the matrix is higher than for cases A or B. Also, it was observed that the smaller pore diameter in case C resulted in a higher flow velocity, leading the front flame to stabilize farther from the entry and the preheat zone to be wider. The preheat efficiency was increased from 43% in case A to 63% in case C.
- Syngas production was evaluated in terms of conversion efficiency and it was observed that a slight improvement from 41 to 43% was obtained with case B. The high local temperature reached in case C allowed to produce higher levels of syngas, resulting in a 10% conversion efficiency gain as compared to case B.
- A graded geometry with a decreasing pore density was simulated for the first time, and promising results were obtained with respect to preheat efficiency and for syngas production. Indeed, the wide preheat zone resulted in a 59% recirculation efficiency, while the conversion of CH_4 to syngas was about 20% higher than in cases A and B.
- Observations of the combustion at the pore scale revealed that the high amount of H_2 produced locally was then mitigated and partially consumed by the RWGS reaction.
- The production of three soot precursors was significantly reduced when burning a rich mixture in the graded geometry. The stretched cells of the matrix form an elongated post-flame zone where the oxidation of three C_2 species studied is possible since all the reactions occur in a single cell.

This study revealed the advantages of using a porous burner having a tailored geometry with a varying pore density. The gains obtained in terms of the preheat efficiency and conversion efficiency were also observed when the matrix porosity was decreased.

Declaration of competing interest

The authors declare that they have no known competing financial interests or personal relationships that could have appeared to influence the work reported in this paper.

Acknowledgements

Chemical species and materials

CH_4	Methane
C_2H_2	Acetylene
C_2H_4	Ethylene
C_2H_6	Ethane
CO	Carbon monoxide
CO_2	Carbon dioxide
H_2	Hydrogen
H_2O	Water
SiSiC	Silicon infiltrated silicon carbide
C_2	Soot precursors (acetylene, ethane and ethylene)

Greek symbols

α	Absorption coefficient
ρ	Density (kg/m^3)
ε	Emissivity
φ	Equivalence ratio
ϕ	Porosity
$\dot{\omega}$	Production/Consumption rate (mol/s^1/m^3)
δ	Scattering coefficient
σ	Stefan-Boltzmann constant
$\underline{\tau}$	Viscous stress tensor (Pa)
λ	Wavelength

Latin symbols

Q_{ch}	Chemical heat release (W/m^3)
h_{conv}	Convective heat transfer coefficient (W/m^2/K)
u_D	Darcy velocity (m/s)
h_k	Enthalpy of the specie k (J/mol)
q	Heat flux (W/m^2)
Y	Mass fraction
W	Molecular weight (kg/mol)
P	Pressure (Pa)
I_b	Radiative intensity (m$^2 \times$ sr/m)
Re_p	Reynolds number based on pore radius
C_s	Solid heat capacity
$D_{k,m}$	Diffusion coefficient between species (m^2/s)
C_P	Specific heat capacity at constant pressure (J/kg/K)
T	Temperature (K)
k	Thermal conductivity (W/m/K)
R	Universal ideal gas constant (J/mol/K)
$\vec{u}$	Velocity vector (m/s)

REFERENCES

[1] Vosloo AC. Fischer-Tropsch: a futuristic view. Fuel Process Technol Jun. 2001;71(1-3):149–55. https://doi.org/10.1016/S0378-3820(01)00143-6.

[2] Abdul Mujeebu M. Hydrogen and syngas production by superadiabatic combustion - a review. Appl Energy Jul. 2016;173:210–24. https://doi.org/10.1016/j.apenergy.2016.04.018.

[3] Zeng H, Wang Y, Shi Y, Ni M, Cai N. Syngas production from CO 2/CH 4 rich combustion in a porous media burner: experimental characterization and elementary reaction model. Fuel Jul. 2017;199:413–9. https://doi.org/10.1016/j.fuel.2017.03.003.

[4] Shi X, Wang F, Cheng Z, Liang H, Dong Y, Chen X. Numerical analysis of the biomimetic leaf-type hierarchical porous structure to improve the energy storage efficiency of solar driven steam methane reforming. Int J Hydrogen Energy May 2021;46(34):17653–65. https://doi.org/10.1016/j.ijhydene.2021.02.171.

[5] Bedoya C. Stationary Flames within Porous Inert Media. Dissertation: Karlsruher Institut für Technologie; 2016. https://doi.org/10.5445/IR/1000052139.

[6] Nourbakhsh H, Rahbar Shahrouzi J, Ebrahimi H, Zamaniyan A, Jafari Nasr MR. Experimental and numerical study of syngas production during premixed and ultra-rich partial oxidation of methane in a porous reactor. Int J Hydrogen Energy Dec. 2019;44(60):31757–71. https://doi.org/10.1016/j.ijhydene.2019.10.084.

[7] Nourbakhsh H, Rahbar Shahrouzi J, Ebrahimi H, Zamaniyan A. Experimental study of ultra-rich thermal partial oxidation of methane using a reticulated porous structure. Int J Hydrogen Energy Apr. 2020;45(22):12298–307. https://doi.org/10.1016/j.ijhydene.2020.02.182.

[8] Dai H, Zhu H, Dai H, Song Z, Wang Z, He S. Syngas production by methane-rich combustion in a divergent burner of porous media. Int J Hydrogen Energy Jul. 2021;46(45):23279–91. https://doi.org/10.1016/j.ijhydene.2021.04.160.

[9] Fay M, Dhamrat R, Ellzey JL. Effect of porous reactor design on conversion of methane to hydrogen. Combust Sci Technol 2005;177(11):2171–89.

[10] Loukou A, Mendes MAA, Frenzel I, Pereira JMC, Ray S, Pereira JCF. Experimental and numerical investigation of methane thermal partial oxidation in a small-scale porous media reformer. Int J Hydrogen Energy Jan. 2017;42(1):652–63. https://doi.org/10.1016/j.ijhydene.2016.11.062.

[11] Wang Y, Zeng H, Shi Y, Cai N. Methane partial oxidation in a two-layer porous media burner with Al2O3 pellets of different diameters. Fuel Apr 2018;217:45–50. https://doi.org/10.1016/j.fuel.2017.12.088.

[12] Shahnazari MR, Moosavi MH, Saberi A. Numerical and experimental investigation of partial oxidation of methane in a porous media to achieve optimum hydrogen production. Energy Sources, Part A Recovery, Util Environ Eff Mar. 2020;42(5):625–40. https://doi.org/10.1080/15567036.2019.1588426.

[13] Mujeebu MA, Abdullah MZ, Mohamad AA, Bakar MZA. Trends in modeling of porous media combustion. Prog Energy Combust Sci Dec. 2010;36(6):627–50. https://doi.org/10.1016/j.pecs.2010.02.002.

[14] Caldeira AB, Susantez C. A simplified numerical approach to hydrogen and hydrocarbon combustion in single and double-layer porous burners. Int J Hydrogen Energy Dec. 2020;45(60):35235–45. https://doi.org/10.1016/j.ijhydene.2020.04.169.

[15] Barra AJ, Diepvens G, Ellzey JL, Henneke MR. Numerical study of the effects of material properties on flame stabilization in a porous burner. Combust Flame 2003;134(4):369–79.

[16] Hashemi SM, Hashemi SA. Flame stability analysis of the premixed methane-air combustion in a two-layer porous media burner by numerical simulation. Fuel 2017;202:56–65.

[17] Shin Y, Kim Y. Numerical modeling for flame dynamics and combustion processes in a two-sectional porous burner with a detailed chemistry. J Mech Sci Technol 2014;28(11):4797–805.

[18] Hoda SN, Nassab SAG, Ebrahim JJ. Three dimensional numerical simulation of combustion and heat transfer in porous radiant burners. Int J Therm Sci 2019;145:106024.

[19] Shi J, Mao M, Li H, Liu Y, Lv J. A pore level study of syngas production in two-layer burner formed by staggered arrangement of particles. Int J Hydrogen Energy Jan. 2020;45(3):2331–40. https://doi.org/10.1016/j.ijhydene.2019.11.017.

[20] Billerot P-L, Dufresne L, Lemaire R, Seers P. 3D CFD analysis of a diamond lattice-based porous burner. Energy Sep. 2020;207:118160. https://doi.org/10.1016/j.energy.2020.118160.

[21] Yakovlev I, Zambalov S. Three-dimensional pore-scale numerical simulation of methane-air combustion in inert porous media under the conditions of upstream and downstream combustion wave propagation through the media. Combust Flame Nov. 2019;209:74–98. https://doi.org/10.1016/j.combustflame.2019.07.018.

[22] Bedoya C, Dinkov I, Habisreuther P, Zarzalis N, Bockhorn H, Parthasarathy P. Experimental study, 1D volume-averaged calculations and 3D direct pore level simulations of the flame stabilization in porous inert media at elevated pressure. Combust Flame 2015;162(10):3740–54.

[23] Wu Z, Wang J, Xie B, Yang J, Wang Q. Methane steam reforming with axial variable diameter particle structures in grille-sphere composite packed bed: a numerical study of hydrogen production performance. Energy Convers Manag 2021;240:114163.

[24] Vahidhosseini SM, Esfahani JA, Kim KC. Cylindrical porous radiant burner with internal combustion regime: energy saving analysis using response surface method. Energy Sep. 2020;207:118231. https://doi.org/10.1016/j.energy.2020.118231.

[25] Vahidhosseini SM, Esfahani JA, Kim KC. Assessment of a cylindrical porous radiant burner with internal combustion regime for sustainable energy: numerical analysis of the radiant efficiency and NO production. Sustain Energy Technol Assessments Feb. 2021;43:100974. https://doi.org/10.1016/j.seta.2020.100974.

[26] Vahidhosseini SM, Esfahani JA, Kim KC. Experimental study on the radiative heat transfer in a multi-hole porous radiant burner with internal combustion regime. Appl Therm Eng Jan. 2022;201:117732. https://doi.org/10.1016/j.applthermaleng.2021.117732.

[27] Samoilenko M, Seers P, Terriault P, Brailovski V. Design, manufacture and testing of porous materials with ordered and random porosity: application to porous medium burners. Appl Therm Eng 2019;158:113724. https://doi.org/10.1016/j.applthermaleng.2019.113724.

[28] Sobhani S, Muhunthan P, Boigné E, Mohaddes D, Ihme M. Experimental feasibility of tailored porous media burners enabled via additive manufacturing. Proc Combust Inst 2021;38(4):6713–22. https://doi.org/10.1016/j.proci.2020.06.120.

[29] Shi X, Xun Y, Dong Y, Wang F, Zhang X, Cheng Z. Analysis of biomimetic hierarchical porous structure regulating radiation field to improve solar thermochemical performance based on minimum Gibbs free energy. Int J Hydrogen Energy 2022, Jan;47(5):2832–45. https://doi.org/10.1016/j.ijhydene.2021.10.246.

[30] Fee C. 3D-printed porous bed structures. Curr Opin Chem Eng Nov. 2017;18:10–5. https://doi.org/10.1016/j.coche.2017.07.003.

[31] Frenklach M, Wang H, Goldenberg M, Smith G, Golden D. Grimech: an optimized detailed chemical reaction mechanism for methane combustion. topical report, september 1992-august 1995. Menlo Park, CA (United States): SRI International; 1995.

[32] Simcenter STAR-CCM+. Siemens gmbh. 2021.

[33] Ergun S, Orning AA. Fluid flow through randomly packed columns and fluidized beds. Ind Eng Chem Jun. 1949;41(6):1179–84. https://doi.org/10.1021/ie50474a011.

[34] Fand RM, Kim BYK, Lam ACC, Phan RT. Resistance to the flow of fluids through simple and complex porous media whose matrices are composed of randomly packed spheres. J Fluid Eng Sep. 1987;109(3):268–73. https://doi.org/10.1115/1.3242658.

[35] Du Plessis P, Montillet A, Comiti J, Legrand J. Pressure drop prediction for flow through high porosity metallic foams. Chem Eng Sci 1994;49(21):3545–53. https://doi.org/10.1016/0009-2509(94)00170-7.

[36] Bubnovich V, Toledo M, Henríquez L, Rosas C, Romero J. Flame stabilization between two beds of alumina balls in a porous burner. Appl Therm Eng Feb. 2010;30(2-3):92–5. https://doi.org/10.1016/j.applthermaleng.2009.04.001.

[37] Barra AJ, Ellzey JL. Heat recirculation and heat transfer in porous burners. Combust Flame Apr. 2004;137(1-2):230–41. https://doi.org/10.1016/j.combustflame.2004.02.007.

[38] Toledo M, Bubnovich V, Saveliev A, Kennedy L. Hydrogen production in ultrarich combustion of hydrocarbon fuels in porous media. Int J Hydrogen Energy Feb 2009;34(4):1818–27. https://doi.org/10.1016/j.ijhydene.2008.12.001.

[39] Pastore A, Mastorakos E. Syngas production from liquid fuels in a non-catalytic porous burner. Fuel Jan. 2011;90(1):64–76. https://doi.org/10.1016/j.fuel.2010.08.003.